MDPI

Article

The Influence of Yttrium Content and Ceramic Crucible Materials on Desulfurization during Vacuum Induction Melting of DD5 Superalloys

Fuwei Wang [1,2], Ying Cheng [1,2,*], Shoubin Zhang [2], Rui Zhang [2], Yanyun Sun [1,2], Kai Guan [3], Huarui Zhang [1,2,*] and Hu Zhang [1,2]

1 Research Institute for Frontier Science, Beihang University, Beijing 100191, China; 18810522297@buaa.edu.cn (Y.S.)
2 Ningbo Institute of Technology (NIT), Beihang University, Ningbo 315000, China
3 Science and Technology of Advanced High-Temperature Structural Materials Lab, Beijing Institute of Aeronautical Materials, Beijing 100095, China
* Correspondence: cying@buaa.edu.cn (Y.C.); huarui@buaa.edu.cn (H.Z.)

Abstract: In this study, the effect of adding different contents of yttrium (Y) during vacuum induction melting in Al_2O_3 and Y_2O_3 crucibles on the purification of DD5 alloys was investigated. The results show that the Y_2O_3 crucible exhibited great crucible stability and an excellent desulfurization effect when melting a Y-containing DD5 alloy. The S content of the alloy was reduced from 5.03 ppm to 1.36 ppm with the addition of 0.50 wt.% Y. Element Y combined with free S in the melt to form the YS phase, which was removed from the condensate shell and slag during the vacuum induction melting (VIM) process. Meanwhile, when the alloy was melted in the Y_2O_3 crucible with 0.50 wt.% Y addition, there was a reduction in S content from 2.77 ppm to 1.36 ppm compared to the Al_2O_3 crucible. Additionally, the loss of Y decreased from 0.12 wt.% to 0.05 wt.%.

Keywords: nickel-based superalloy; purification; desulfurization; Y_2O_3 crucible

check for **updates**

1. Introduction

DD5 nickel-based superalloy is widely used in high-temperature components such as turbine blades and guide vanes of advanced aero-engines due to its excellent high-temperature mechanical properties and corrosion resistance [1,2]. As aero-engines continue to develop, more demands are being placed on alloys in terms of service temperatures and high-temperature performance [3,4]. In particular, the oxidation resistance and mechanical properties of the material at high temperatures become the main factors limiting the service life of the alloy [5]. Many studies have shown that the addition of yttrium (Y) is conducive to the improvement of high-temperature oxidation resistance and high-temperature creep resistance [6–8]. Y shows a broad application prospect in nickel-based superalloys [9].

It has been known that trace amounts of impurity elements in superalloys can lead to the formation of inclusions that can adversely affect the creep and durability of superalloys, such as O, N, and S [9–11]. Especially, the role of S as an element in the impurities involved in superalloys has received a great deal of attention, because ppm levels of S still have a detrimental effect on the high-temperature properties of the alloys, which in turn affects the performance of superalloy engine parts [12]. Dong et al. [13] reported that when the S content of the In718 alloy was increased from 15 ppm to 50 ppm, the elongation of the alloy decreased from 10 percent to 5 percent. Meanwhile, Sun et al. [14] reported that when the S content of the K24 alloy was increased from 20 ppm to 220 ppm, the UTS of the alloy at 900 °C decreased by about 300 MPa. It can be observed that S in superalloys reacts with nickel-based alloy components to form non-metallic sulfide inclusions. These inclusions include S-containing MC and $M_{23}C_6$ (M: Ni, Cr), as well as compounds like Ni-La-S and

Y_2O_2S, which tend to accumulate at the boundaries of grains or phases [12–14]. These reactions ultimately result in the degradation of the mechanical properties of the alloys at elevated temperatures [15–17]. Therefore, ensuring desulfurization during the preparation process is crucial to maintain the high-temperature performance of superalloys.

At present, the desulfurization methods employed include hydrogen annealing, electroslag remelting (ESR), crucible vacuum induction melting (VIM), and other technologies [18,19]. Among these methods, VIM is the primary preparation process utilized for nickel-based superalloys due to its excellent purification and homogenization effects [20,21]. At the same time, CaO and MgO exhibit exceptional desulfurization capabilities based on the standard Gibbs free energy of the formation of metal sulfides as a function of temperature [15,22]. Li et al. [23] investigated that the S content in Ni-Cr alloys could be reduced from 32 ppm to 11 ppm when using a MgO crucible with the addition of 0.14 wt.% Ce. Similarly, Wang et al. [24] found that S content in the K417G alloy was reduced from 7 ppm to 2 ppm when using a CaO crucible with Ca addition. However, the addition of Y to the VIM process of superalloys presented several limitations. The presence of reactive elements, such as Y, in the melt can result in significant reactions with conventional crucible materials like MgO and CaO, especially under high temperatures and extended melting conditions. These reactions can lead to undesirable effects, such as chemical interactions, dissolution of crucible materials, or formation of compounds that may affect the purity and stability of the melt [25–27]. Consequently, this resulted in the loss of Y and the introduction of impurities, leading to a shorter crucible lifespan and degradation of alloy properties [28]. Therefore, a suitable crucible material must be selected when preparing Y-containing nickel-based superalloys by VIM.

Previous studies have demonstrated that Y_2O_3 crucibles exhibit higher chemical stability and better purification properties compared to conventional ceramic refractories. According to Zhang et al. [29], Y_2O_3 crucibles could attenuate the interfacial reaction between the alloy and the crucible and are ideal for melting superalloys containing reactive elements such as Y, Ti, and Hf. Li et al. [30] reported that using a Y_2O_3 crucible for melting nickel-based superalloys could reduce the S content from 28 ppm to 6–7 ppm, and with the addition of 0.8 wt.% Y, the S content was further reduced to 2–3 ppm. Recent studies have also shown that using a Y_2O_3 crucible for VIM of Y-containing nickel-based superalloys can reduce the S content and is beneficial for the purification process of the alloys [31,32]. However, there are few reports regarding the role of the Y in the desulfurization mechanism and its interfacial reaction with ceramics during the VIM process of the DD5 nickel-based superalloy.

The aim of this study is to investigate and compare the interfacial reaction behavior and thermodynamic conditions of DD5 nickel-based superalloys with different Y contents using two different ceramic crucibles (Y_2O_3 and Al_2O_3) in the VIM process. The focus of the study is to elucidate the reaction mechanisms involving Y and S during the melting of DD5 nickel-based superalloys. Additionally, the study also considers the reaction process between Y and the ceramic crucible. This study has significant implications for the purification of Y-containing DD5 alloys during practical preparation.

2. Experiment

The alloys used in the experiments were designed with specific chemical compositions in weight percent (wt.%), including varying Y additions, as presented in Table 1. The alloy without added Y was labeled as M00. Alloys with Y additions of 0.05 wt.%, 0.15 wt.%, 0.30 wt.%, 0.50 wt.%, 1.50 wt.%, and 4.00 wt.% were melted in Y_2O_3 crucibles, and they were, respectively, marked as Y005, Y015, Y03, Y05, Y15, and Y40. Additionally, alloys with Y additions of 0.50 wt.%, 1.50 wt.%, and 4.00 wt.% were melted in Al_2O_3 crucibles and marked as Al05, Al15, and Al40, respectively.

The Y_2O_3 and Al_2O_3 crucibles utilized in the experiment were made from 99% pure Y_2O_3/Al_2O_3 ceramic particles using the cold isostatic pressing method. The cold isostatic pressing process involved applying a pressure of 180 MPa to compact the ceramic particles.

Following the compaction, the crucibles underwent sintering in a high-temperature vacuum resistance furnace.

Table 1. Nominal components of DD5 superalloys (wt.%).

C	Mo	Al	Co	Hf	Re	Ta	W	Cr	Y	Ni
0.05	1.51	6.16	7.56	0.14	2.91	6.52	5.23	6.93	0-4	Bal

The alloys were prepared by melting in a 100 KW ZG125C VIM furnace (Beijing, China). The alloy was refined for 10 min in a ceramic crucible selected with Y_2O_3 or Al_2O_3 at 2.0×10^{-1} Pa, 1600–1650 °C. Then, the melt was cooled to 1450 °C, rare earth Y element was added, and the substance was homogenized at 1500 °C for 8–10 min. The alloy was cast at 1550 °C into a 50 mm diameter steel mold with a ceramic filter at the pouring gate.

In order to investigate the purification mechanism of Y within the melt and explore the interaction between the Y-containing alloy melt and the ceramic crucible, samples of residual alloy and solid slag were collected from various locations on the crucible and filter surfaces. Metallographic samples were collected from the bottom of the billet for characterization, and composition test samples were collected for chemical analysis. The S content was determined by combustion–infrared absorption method with reference to GB/T20123-2006 using CS-2800 equipment (NCS TESTING TECHNOLOGY CO., LTD., Beijing, China) with an accuracy of $\pm 1 \times 10^{-8}$ [33]. The Y content was analyzed using the inductively coupled plasma (ICP) method. The sample was dissolved, and the resulting solution was compared to a known standard. This comparison was performed in a plasma flame emission spectrometer, which provided an accuracy of $\pm 5 \times 10^{-6}$. To ensure the accuracy of the experimental results, each specimen underwent testing and analysis in at least three parallel replicates. The microstructure and composition were analyzed by ZEISS EV0 (Zeiss, Jena, Germany) scanning electron microscope (SEM) and combined energy dispersive spectrometer (EDS). The phase composition was tested using D/MAX2500pc X-ray diffraction (XRD) (Rigku XRD, Tokyo, Japan) at a scanning angle of 20–100°.

3. Results

3.1. S Content

Figure 1 shows the S content in DD5 alloys with varying Y content prepared through the VIM process using Al_2O_3 and Y_2O_3 crucibles. Originally, without the addition of Y, the S content in the alloy was 5.03 ppm. When the Al_2O_3 crucible was employed for melting the alloys, the S content decreased as Y was added. As the Y content reached 1.50 wt.%, the S content decreased to 1.50 ppm and subsequently stabilized. Similarly, when the Y_2O_3 crucible was used, the S content exhibited a similar trend as observed in the Al_2O_3 samples. When the Y content reached 0.50 wt.%, the S content decreased to 1.36 ppm and then approached a stable level.

3.2. Microstructure

Figure 2 displays the microstructure of the DD5 alloy obtained by adding different Y elements during the melting process in this study. The EDS results for Figure 2 are presented in Table 2. The results revealed the precipitation of white carbides and dark grey Y-rich phases within the matrix. The primary alloying component of the carbides is Ta, accompanied by small quantities of Ni, Mo, and W. And in the Y-rich phase, the main components are Ni and Y, and there are also traces of Al, Cr, and Co. With the addition of Y, the morphology of the white carbide phases precipitated between the dendrites exhibited a gradual shift from continuous, fine granular, and island-like structures to blocky shapes. Additionally, the dark grey Y-rich phases were observed between the dendrites of the Y-containing alloys. The Y-rich phases underwent transformations from fine, massive structures to elongated needles and islands as the Y content increased.
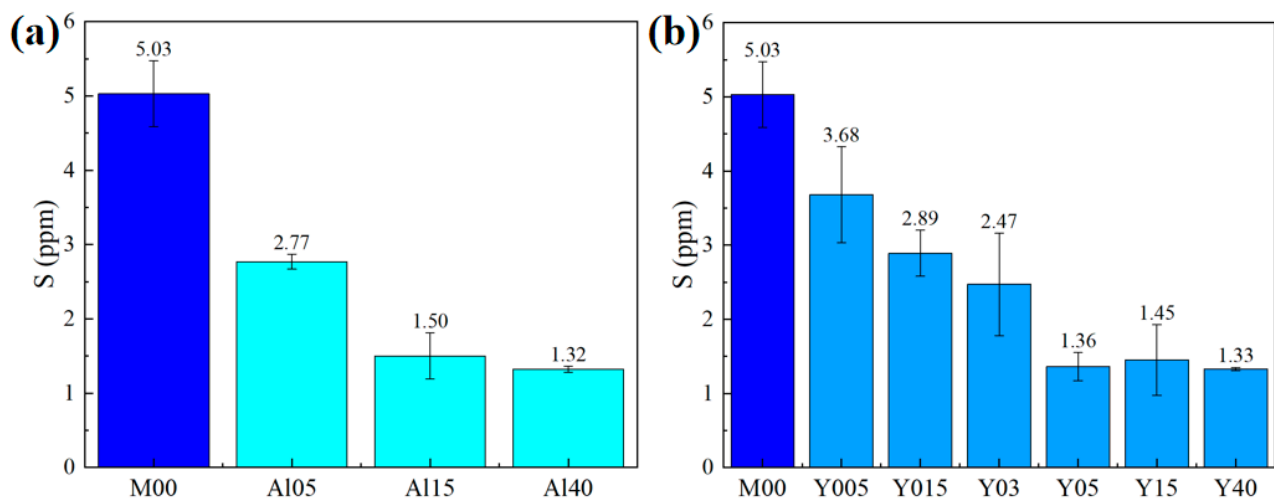
Figure 1. S content in samples with different Y additions in different crucibles: (**a**) Al_2O_3 crucible, (**b**) Y_2O_3 crucible.
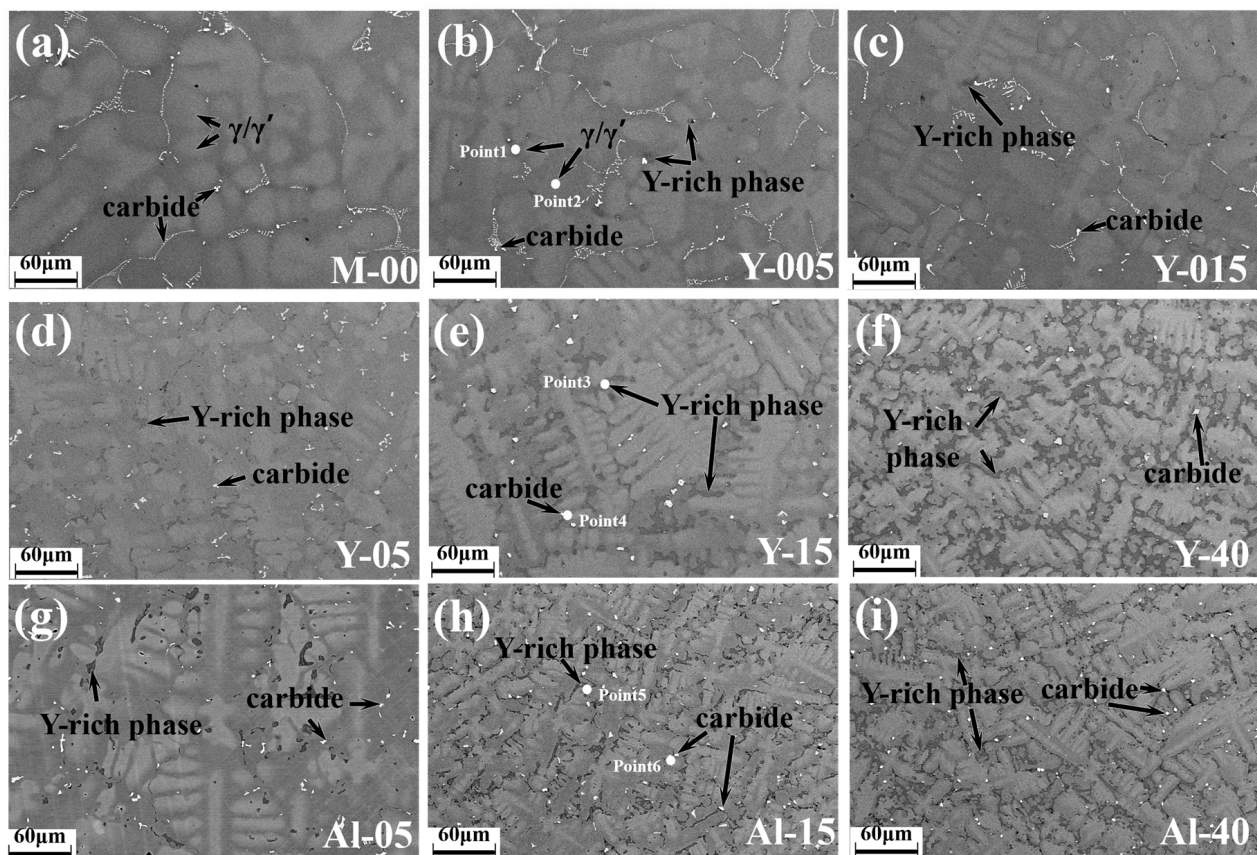

Figure 2. Microstructures of DD5 alloys with different Y contents: (**a**) M00, (**b**) Y005, (**c**) Y015, (**d**) Y05, (**e**) Y15, (**f**) Y40, (**g**) Al05, (**h**) Al15, (**i**) Al40.

The XRD peak spectra of the specimens prepared by the Al_2O_3 crucible and the Y_2O_3 crucible are shown in Figure 3. In these peak spectra, the reinforcing phase γ' was mainly composed of the Ni_3Al phase, the carbides were primarily the MC (TaC, MoC, and WC) carbides [34,35], and the precipitated phases of Y consist of M_5Y (($Al_{0.15}Co_{0.1}Cr_{0.04}Ni_{0.71})_5Y$ and Ni_5Y).

Table 2. EDS results for Figure 2.

wt%	C	Al	Y	Mo	Cr	Co	Ni	Ta	W	Re
Point 1		6.14	0.64	0.61	6.61	7.78	62.00	6.54	9.69	
Point 2		6.82		1.04	6.81	7.09	62.02	8.97	4.12	3.23
Point 3		6.06	17.90		1.92	3.86	70.25			
Point 4	11.95			2.19	1.48		6.36	72.19	5.85	
Point 5		6.65	15.79		3.29	4.68	69.59			
Point 6	13.78	0.41		2.69	2.08	0.64	6.18	69.05	5.17	
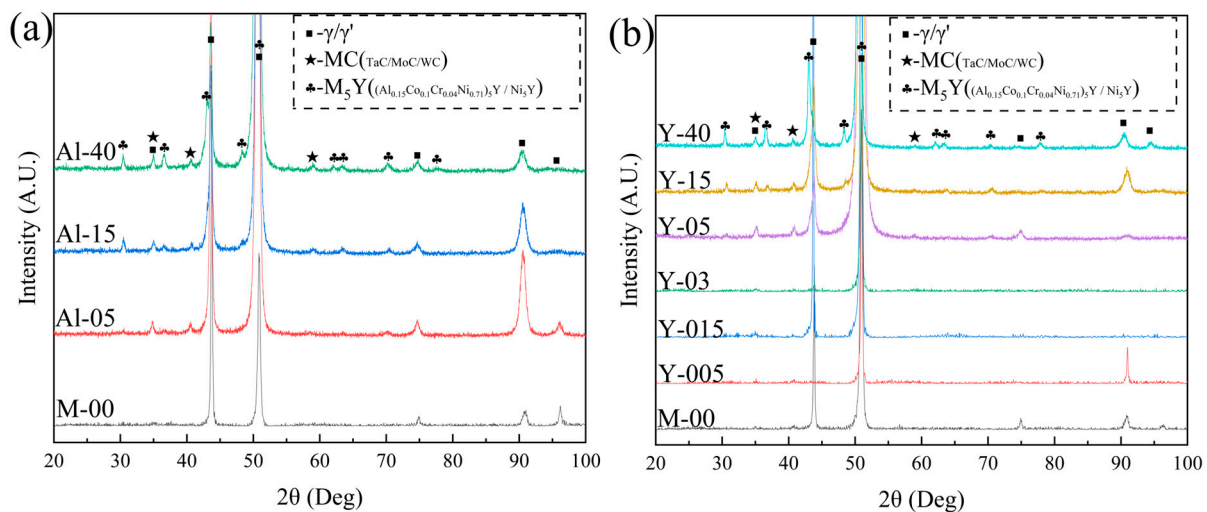
Figure 3. Analysis of the internal phases of the alloy: (**a**) alloys melted in Al_2O_3 crucible, (**b**) alloys melted in Y_2O_3 crucible.

3.3. Interface Reaction

Figure 4 shows the micromorphology of the interfacial reaction layer between the Al_2O_3 crucible and the Al05 sample. It exhibited the diffusion of O from the Al_2O_3 crucible into the alloy, indicating the presence of an interfacial reaction layer. The main component of this reaction layer at the interface between the Al_2O_3 crucible and Al05 sample was a Cr-rich oxide. Additionally, the Y element was found to be enriched in the interfacial reaction layer, particularly in the region closer to the molten side.

After the casting process in the VIM, the remaining metal in the ceramic crucible formed a condensed shell on the inner surface as it cooled down. Figure 5 shows the micromorphology of the inner surface of the Al_2O_3 crucible for melting Al05. It could be seen that a Y-rich phase, resembling a bud, was observed attached to the crucible's inner surface. The presence of a spherical Ni alloy was identified on the surface of the Y-rich phase shell.

Additionally, a Cr-rich phase was found beneath the Y-rich phase, both of which formed a metal shell layer on the inner surface of the Al_2O_3 crucible for melting the Al05 sample. The Cr-rich phase adhered to the inner surface of the crucible in the form of needles, short sticks, or particles. These observations showed that the Cr-rich phase directly adhered to the Al_2O_3 crucible matrix, and it was believed that elemental Cr might participate in the crucible dissolution process as a mediator.

Figure 6 displays the micromorphology of the interfacial reaction layer between the Y_2O_3 crucible and the Y05 sample. The results indicate that the Y_2O_3 ceramics had an alloy bond on the surface, which exhibited a composition matching that of the DD5 alloy. Furthermore, no interfacial reaction zone was observed between the alloy and ceramic.
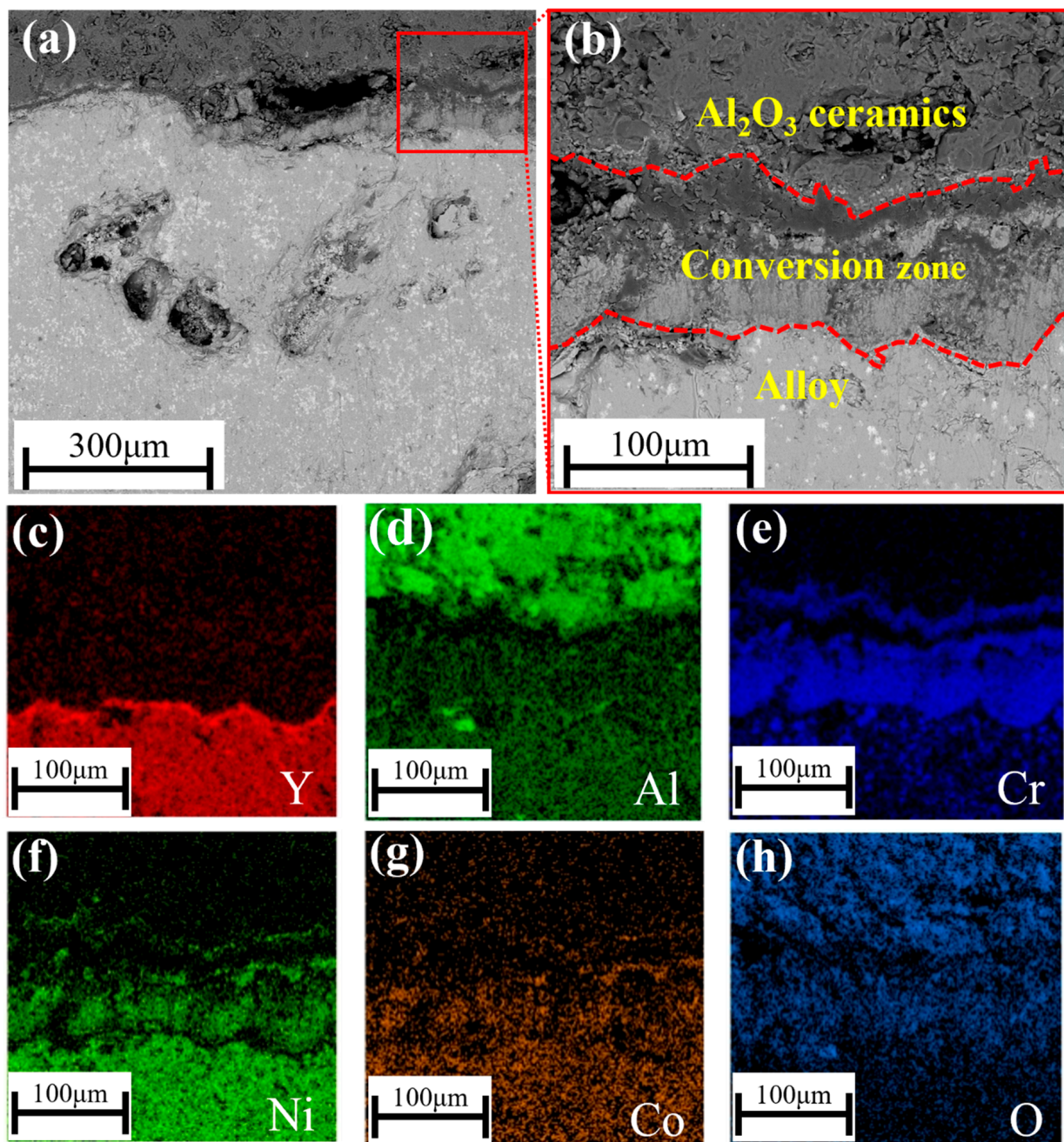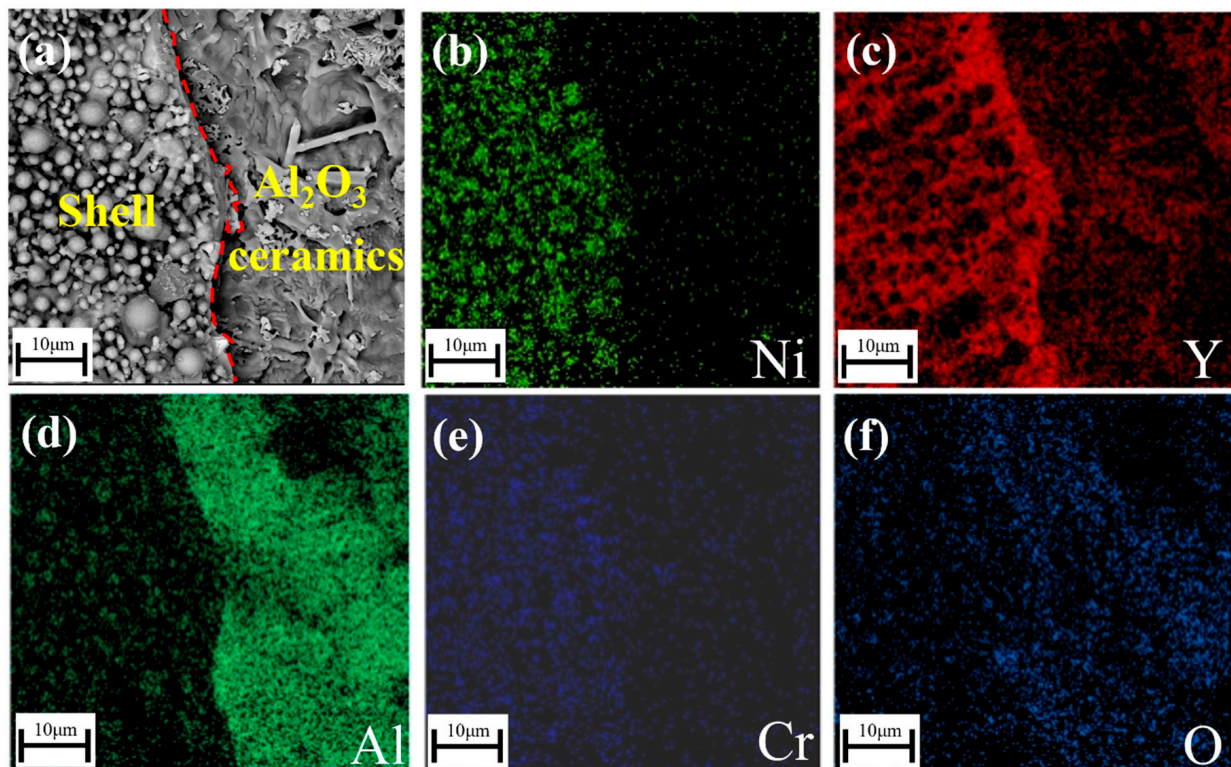
Figure 4. Interfacial morphology between the Al_2O_3 crucible and the Al05 sample: (**a**) low-magnification SEM image, (**b**) high-magnification SEM image. Element distribution of (**c**) Y, (**d**) Al, (**e**) Cr, (**f**) Ni, (**g**) Co, and (**h**) O.
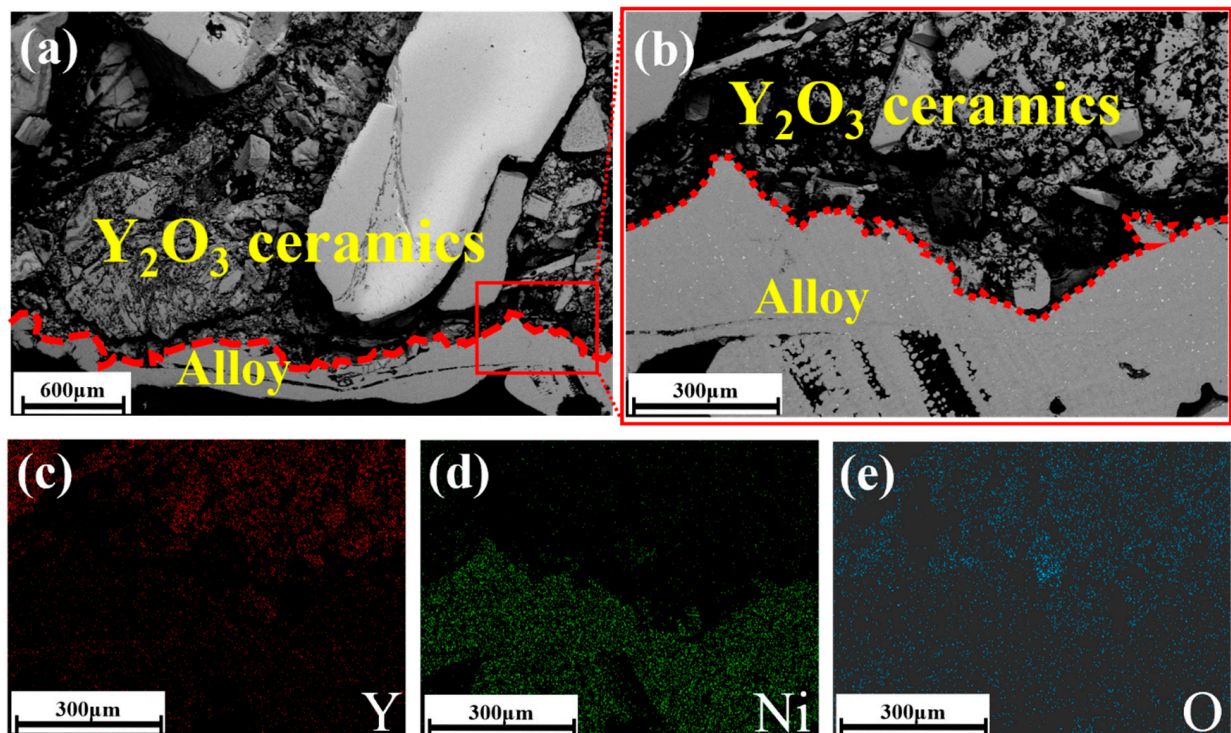
3.4. Slag and Condensation Shell

The slag from the Y05 and Al05 samples, as well as the alloy condensation shells adhering to the inner surface of the crucible in the Y05 and Al05 samples, were collected and subjected to analysis.

The micromorphology of the condensation shell on the inner surface of the Al_2O_3 crucible in the Al05 sample is shown in Figure 7. It was found that the Al-rich phase, Cr-rich phase, and Y-rich phase appear sequentially on the inner surface of the Al_2O_3 crucible. Trace amounts of S were detected in the Y-rich condensate shell, as seen in Figure 7b. Based on the observations from Figures 4 and 7, the composition of the Cr-rich zone revealed the presence of elements such as Ni, Al, Co, Cr, and O.
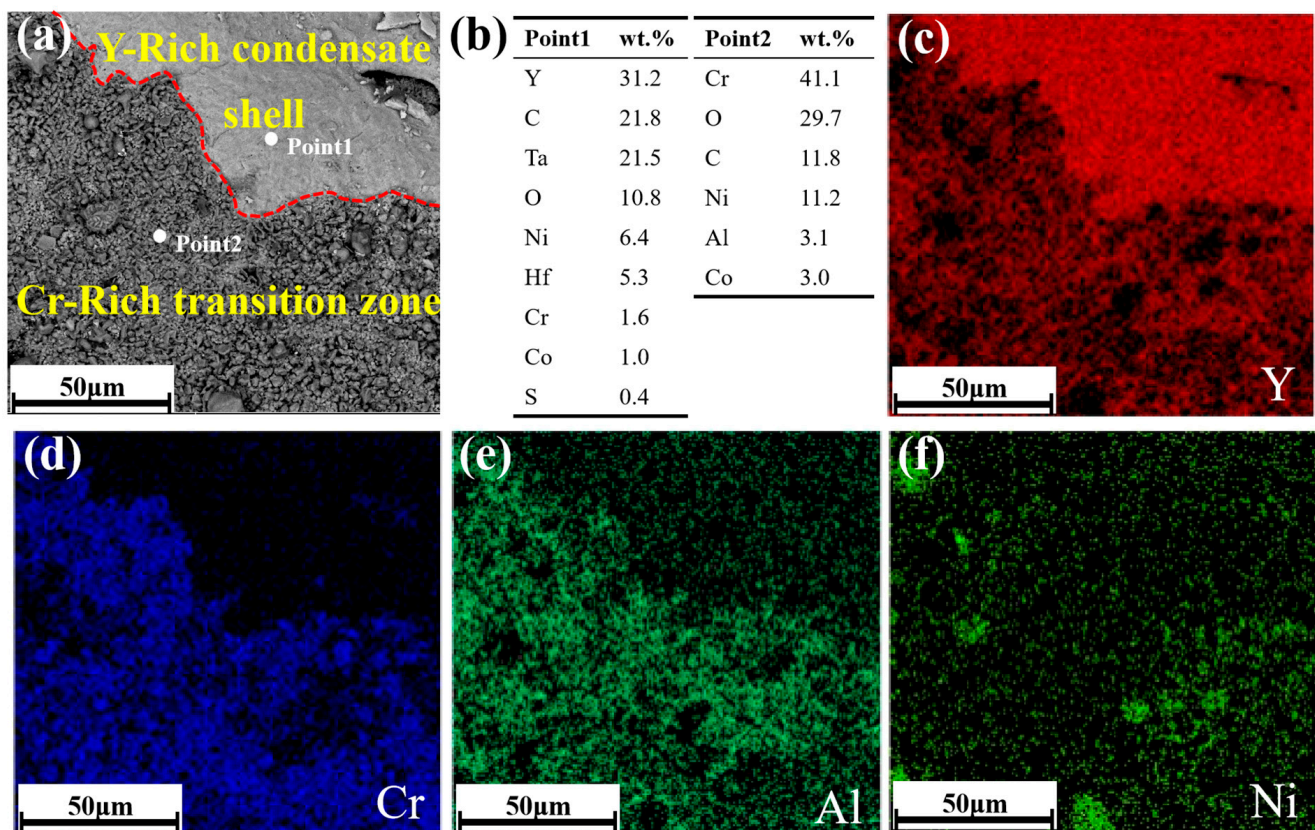
Figure 5. Micromorphology of the inner surface of Al_2O_3 crucible for melting Al05: (**a**) SEM image. Element distribution of (**b**) Ni, (**c**) Y, (**d**) Al, (**e**) Cr, and (**f**) O.

Figure 6. Interfacial morphology between the Y_2O_3 crucible and the Y05 sample: (**a**) low-magnification SEM image, (**b**) high-magnification SEM image. Element distribution of (**c**) Y, (**d**) Ni, and (**e**) O.

Figure 7. Micromorphology of the condensation shell on the surface of Al_2O_3 crucible in the Al05 sample: (**a**) SEM image. (**b**) EDS results for subfigure (**a**). Element distribution of (**c**) Y, (**d**) Cr, (**e**) Al, and (**f**) Ni.

Figure 8 shows the micromorphology of the condensation shell on the inner surface of the Y_2O_3 crucible in the Y05 sample. The results indicate that the nickel-based superalloy was observed on the surface of the Y_2O_3 crucible after the separation of the Y-rich condensation shell. In Figure 8b, trace amounts of S were found in the Y-rich condensation shell on the surface of the Y_2O_3 crucible. Additionally, the weight percentage of Y in the Y-rich condensation shell increased compared to that in the Al_2O_3 crucible sample.

The XRD peak spectra of the alloy condensation shells on the crucible surface of the Al05 and Y05 samples are shown in Figure 9. The results indicate the presence of Y_2O_3 and oxide phases such as Y-Al, Y-Mo, and Y-Al-Cr on the surface of the Al05 condensation shell. And the S-containing phase in the Al05 condensation shells was identified as the MS (M: Y, Cr) phase. Furthermore, analysis reveals the presence of Y_2O_3, TaO, and Y-Mo oxide phases on the surface of the Y05 condensation shell. And the S-containing phase in the Y_2O_3 condensation shell was identified as the YS phase.

Figure 10 shows the surface morphology of the slags, while Figure 11 displays the XRD peak spectrum of the slags collected during melting using Al_2O_3 and Y_2O_3 crucibles. The results reveal the presence of an MS (M: Y, Cr) phase in the Al05 slag. This MS phase was found to be formed within the M_5Y phase, with a small size of only 0.5 μm in the Al05 slag. Meanwhile, the Al05 slag contained oxides of Y, Cr, and Al, as well as binary oxides of Y-Cr and Y-Mo and ternary oxides of Y-Cr-Al. On the other hand, the Y05 slag exhibited the presence of the YS phase. At the same time, oxides of Y and Ta, as well as binary oxides of Y-Mo, were observed in the Y05 slag.
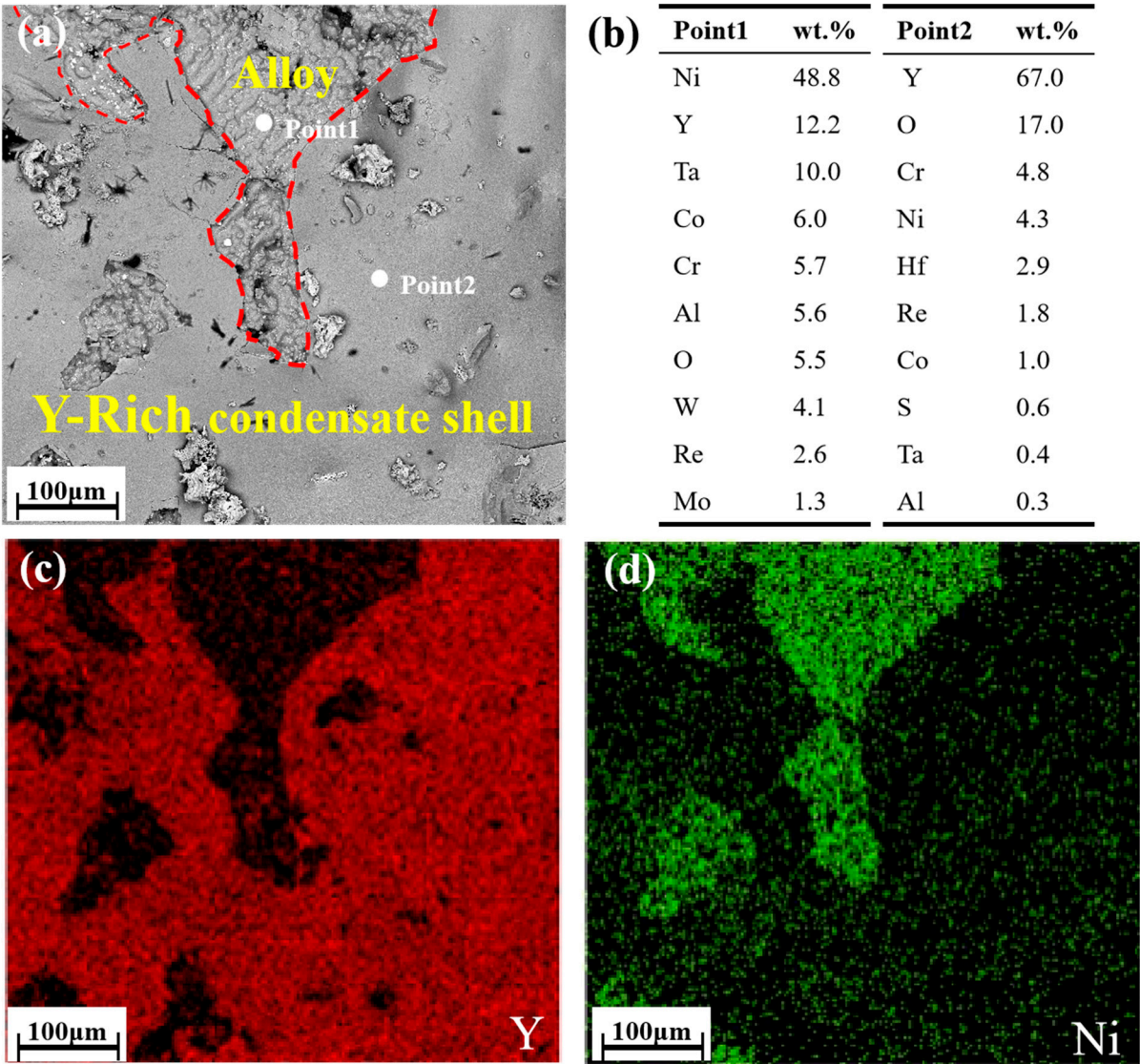
Point1	wt.%	Point2	wt.%
Ni	48.8	Y	67.0
Y	12.2	O	17.0
Ta	10.0	Cr	4.8
Co	6.0	Ni	4.3
Cr	5.7	Hf	2.9
Al	5.6	Re	1.8
O	5.5	Co	1.0
W	4.1	S	0.6
Re	2.6	Ta	0.4
Mo	1.3	Al	0.3

Figure 8. Micromorphology of the condensation shell on the surface of Y_2O_3 crucible in the Y05 sample: (**a**) SEM image, (**b**) EDS results for subfigure (**a**). Element distribution of (**c**) Y and (**d**) Ni.
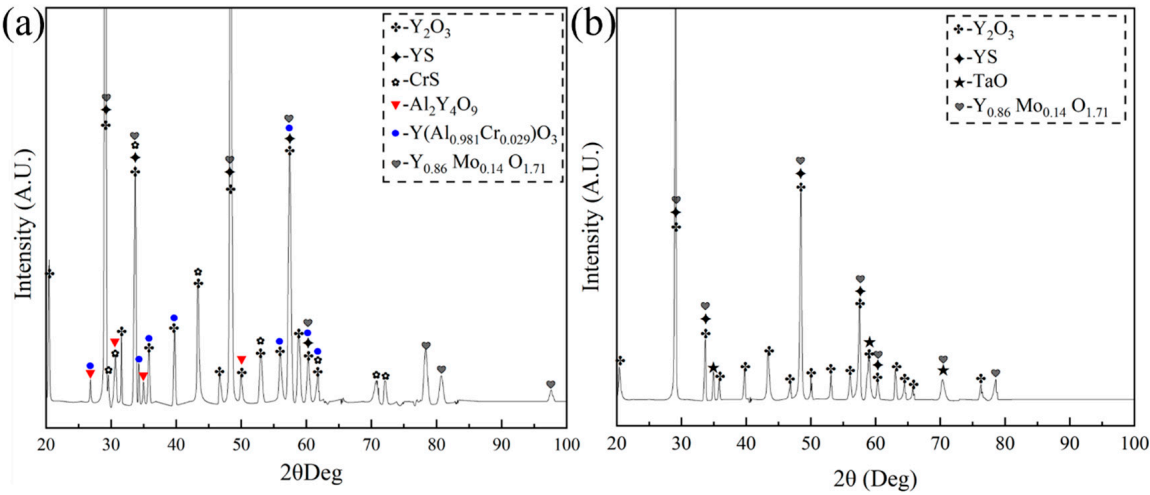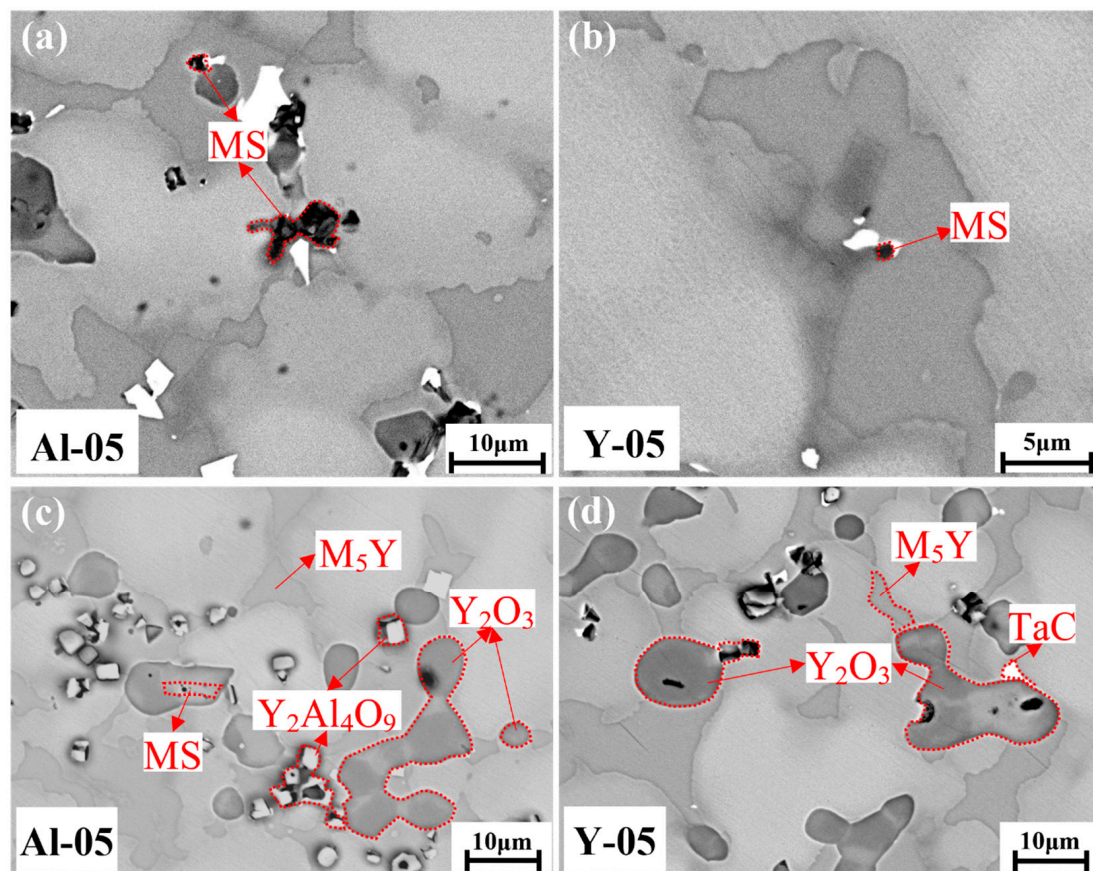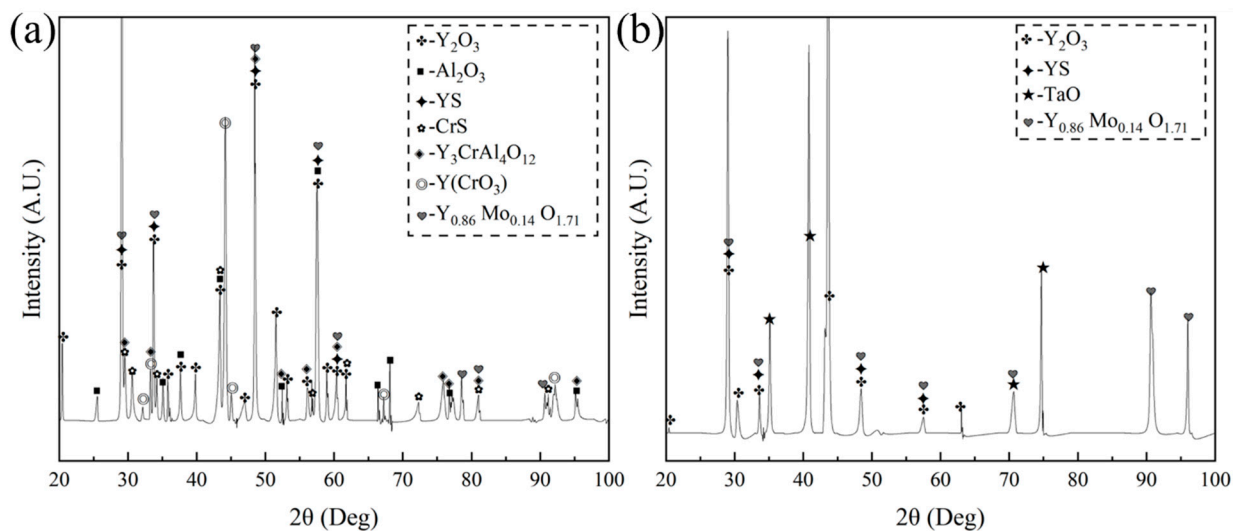

Figure 9. XRD analysis of condensation shell on the surface of ceramic crucible: (**a**) Al05 sample, (**b**) Y05 sample.

Figure 10. Micromorphology of Al_2O_3 crucible and Y_2O_3 crucible slag: (**a**,**c**) SEM image of Al05 sample. (**b**,**d**) SEM image of Y05 sample.

**Figure 11.** XRD analysis of slag: (**a**) Al05 sample, (**b**) Y05 sample.

The nominal and actual compositions of Y in different alloy samples are shown in Table 3. The Y addition refers to the amount of Y intentionally added during the experiment, while the Y content in each sample was determined using ICP analysis, which represents the measured concentration of Y. The results show that when equal amounts of Y were added, the burning loss of Y element in melting DD5 superalloys using an Al_2O_3 crucible was much higher than that when the Y_2O_3 crucible was used.

Table 3. Addition and actual composition of Y in the alloys.

	Y Addition (wt.%)	Y Content (wt.%)	ΔY (wt.%)		Y Addition (wt.%)	Y Content (wt.%)	ΔY (wt.%)
Y00	0	<0.0001	-	Y15	1.50	1.32	−0.18
Y005	0.05	0.06	0.01	Y40	4.00	3.44	−0.56
Y015	0.15	0.12	−0.03	Al05	0.50	0.38	−0.12
Y03	0.30	0.22	−0.08	Al15	1.50	1.28	−0.22
Y05	0.50	0.45	−0.05	Al40	4.00	2.45	−1.55

ΔY = Y content − Y addition(wt.%).

Figure 12 shows the S content in the alloys, slags, and condensation shells bonded to the inner surface of the Y_2O_3 or Al_2O_3 crucible for the Y05 and Al05 samples.
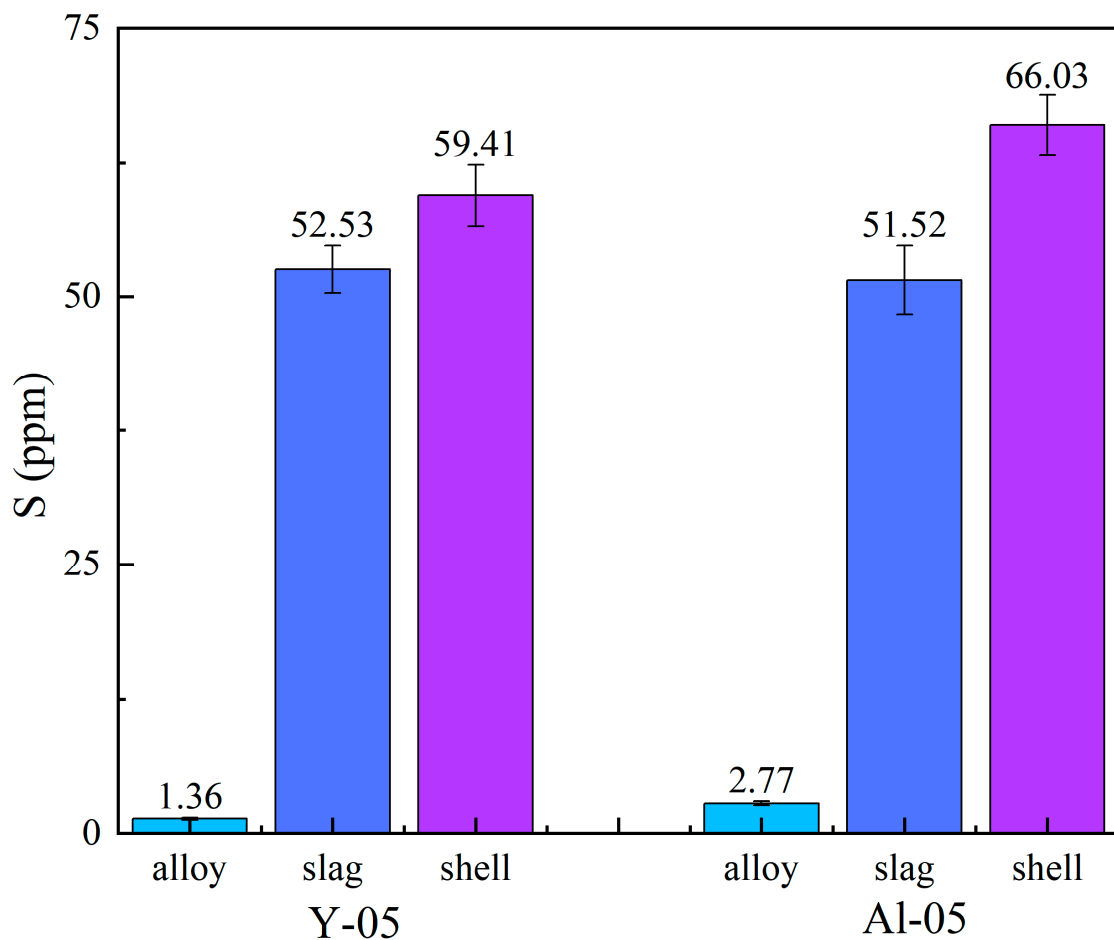
Figure 12. S content in alloys, slags, and condensate shells bonded to the inner surface of Y_2O_3 or Al_2O_3 crucible of Y05 and Al05 samples.

The results suggest that the S contents in the slag and condensation shells of the Y_2O_3 and Al_2O_3 crucibles were much higher than that in the alloy. Specifically, the S contents in the crucible slag and condensation shells were found to be approximately 20–40 times higher than the S contents in the alloy matrix.

4. Discussion

4.1. Mechanism of Desulfurization

The desulfurization process of DD5 superalloy can be divided into three stages. The first stage is the rapid desulfurization process that occurs at high temperatures, under high vacuum conditions, and with electromagnetic stirring in the early stage of melting. During

this stage, S is rapidly removed from the alloy. The second stage is crucible desulfurization, which takes place in the late stage of melting. In this stage, the crucible itself plays a role in absorbing and removing S from the alloy. The third stage is deep desulfurization during the refining stage, where Y is used as a refining agent. Y interacts with S in the alloy, forming YS compounds that can be removed from the melt, thereby achieving deeper desulfurization [30].

According to Figure 1, the S content gradually decreased with the addition of Y and eventually reached a stable level when using the Y_2O_3 or Al_2O_3 crucible for preparation. This phenomenon can be attributed to the fact that Y, being an active element, readily combines with S in the alloy, forming slag that can be removed. Table 3 provides further evidence, showing that as the amount of Y added increases, more Y elements participate in the removal of S. Meanwhile, the S content exhibited a tendency to stabilize when an adequate amount of Y was added.

As can be seen from Figure 11, the S contents in the slag and condensed shell were much higher than that in the alloy of Y05 and Al05 samples. The mechanism of S removal in the DD5 alloy primarily involves a deep desulfurization process facilitated by Y. During this stage, monomeric Y directly combines with S in the melt, resulting in the formation of YS compounds [36].

$$[Y]Ni(l) + [S]Ni(l) = YS(s) \tag{1}$$

Y and Cr in the alloy melt reacted with the Al_2O_3 crucible during the melting of Y-containing DD5 alloys using the Al_2O_3 crucible, forming polyoxides such as Y_2O_3 and $Al_2Y_4O_9$, among others, and sulfides (MS, M: Y/Cr) [9,37]. The depletion of Y due to these reactions could have implications for the deep desulfurization process during the refining of the Y-containing alloy.

$$Al_2O_3(s) + [Cr]Ni(l) + [S]Ni(l) + [Y]Ni(l) = CrS(s) + YS(s) + Al_xY_yCr_zO_m(s/l) \tag{2}$$
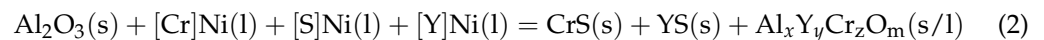
4.2. Interfacial Reaction

The micromorphology results of the Al_2O_3 crucible (Figures 4, 5 and 7) and the XRD analysis results of the condensate shell and alloy slag of the Al_2O_3 sample (Figures 9 and 11) were used to explain the substitution reaction between Y and Al_2O_3 and the formation reactions of different oxides occurring at the interface of the crucible during VIM melting of Y-containing DD5 alloys in the Al_2O_3 ceramic crucible, as illustrated in Figure 13a.
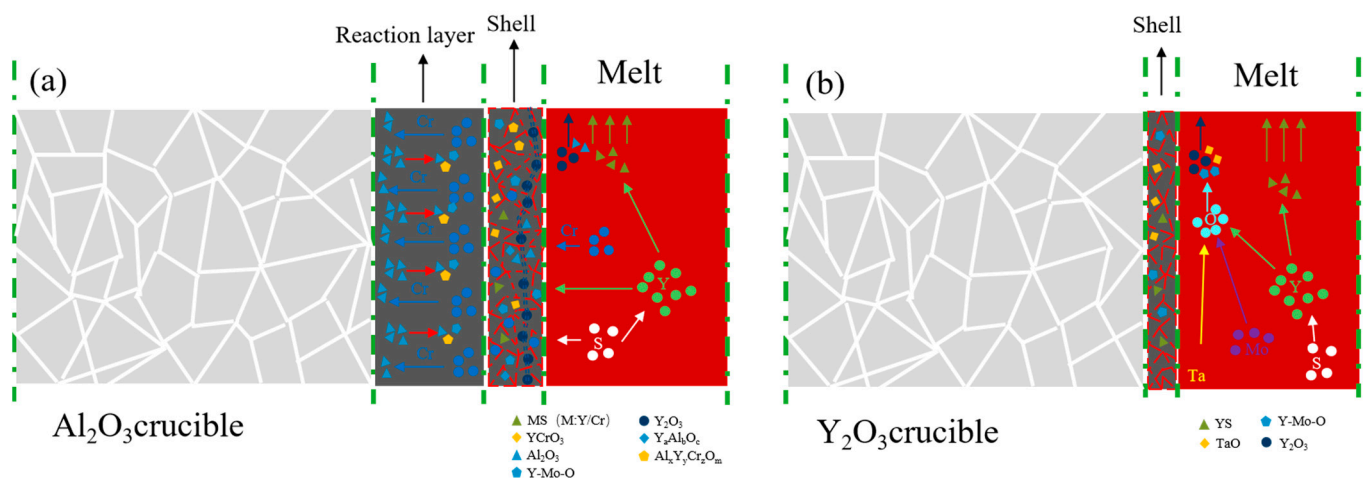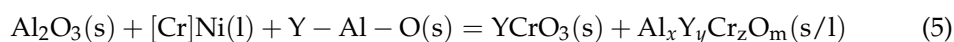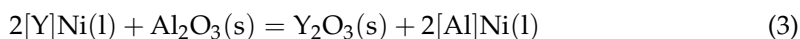

Figure 13. Interface reaction diagram of Y-containing alloy with different crucibles: (**a**) Al_2O_3 crucible, (**b**) Y_2O_3 crucible.
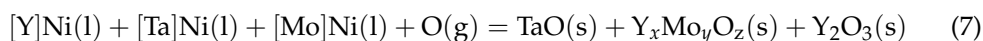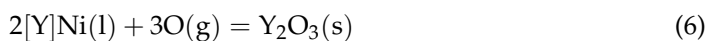
According to the research, we thought that the Y in the alloy reacted with the Al_2O_3 crucible due to its high reactivity. Part of the Y oxidized to Y_2O_3 and part of it combined

with Al_2O_3 to form Y-Al binary oxides such as $Al_2Y_4O_9$ [38]. The Y_2O_3 and Y-Al binary oxides generated from these interfacial reactions were deposited on the inner surface of the Al_2O_3 ceramic crucible, forming a Y-rich phase condensation shell. Subsequently, the Cr element acted as a mediator, penetrating the Y-rich phase condensation shell and continuing to react with the Al_2O_3 crucible. This reaction formed the $Al_xY_yCr_zO_m$ (s/l) ternary oxide, further promoting the ongoing reaction between Y in the alloy and the Al_2O_3 crucible [16,17].

$$2[Y]Ni(l) + Al_2O_3(s) = Y_2O_3(s) + 2[Al]Ni(l) \tag{3}$$

$$Al_2O_3(s) + 2Y_2O_3(s) = Al_2Y_4O_9 \ (s) \tag{4}$$

$$Al_2O_3(s) + [Cr]Ni(l) + Y - Al - O(s) = YCrO_3(s) + Al_xY_yCr_zO_m(s/l) \tag{5}$$

Based on the SEM analyses of the Y_2O_3 sample (Figures 6 and 10) and the XRD analyses of the condensation shell and slag of the Y_2O_3 sample (Figures 9 and 11), it can be observed that the Y oxide ceramic crucible underwent reactions leading to the production of multiple oxides during the VIM melting of Y-containing DD5 alloys, as depicted in Figure 13b.

$$2[Y]Ni(l) + 3O(g) = Y_2O_3(s) \tag{6}$$

$$[Y]Ni(l) + [Ta]Ni(l) + [Mo]Ni(l) + O(g) = TaO(s) + Y_xMo_yO_z(s) + Y_2O_3(s) \tag{7}$$

On the experimental basis, it was found that the Y_2O_3 crucible did not directly react with the alloy melt during melting of Y-containing DD5 alloys using the Y_2O_3 crucible due to their elevated temperature property [39]. However, the reactive elements in the melt reacted with the remaining O in the atmosphere or were released during crucible dissolution. This resulted in the formation of Y and Ta oxides, as well as Y-Mo binary oxides. Some of these oxides formed a solid phase on the surface of the Y_2O_3 crucible and remained in the condensation shell, while others were removed with the slag.

5. Conclusions

In this study, the purification melting mechanism of the Y-containing DD5 alloy and its interfacial reaction law with the ceramic crucible during the VIM process were investigated. The main conclusions are as follows:

(1) Y played an important role in the purification process of DD5 alloy VIM. When melted in the Y_2O_3 crucible, the S content of the alloy was reduced from 5.03 ppm to 1.36 ppm with the addition of 0.50 wt.% of Y. Meanwhile, when melted in the Al_2O_3 crucible, the S content of the alloy was reduced from 5.03 ppm to 1.32 ppm with the addition of 4.00 wt.% of Y. Element Y combined with free S in the melt to form the YS phase, which was removed from the condensate shell and slag during the VIM process.

(2) The Y_2O_3 crucible exhibited great crucible stability and an excellent desulfurization effect when melting Y-containing DD5 alloy. When the alloy was melted in the Y_2O_3 crucible with 0.50 wt.% Y addition, there was a reduction in S content from 2.77 ppm to 1.36 ppm compared to the Al_2O_3 crucible. Meanwhile, the loss of Y also decreased from 0.12 wt.% to 0.05 wt.%.

(3) Y-containing DD5 alloys underwent interfacial reactions with the crucible when prepared by VIM in an Al_2O_3 crucible. The oxides such as Y_2O_3 and $Al_2Y_4O_9$ generated from the interfacial reaction were deposited on the surface of Al_2O_3 ceramics to form a Y-rich phase condensate shell, and Cr acted as a mediator to penetrate the Y-rich phase condensate shell, which caused the interfacial reaction to continue and generated $Al_xY_yCr_zO_m$ (s/l) ternary oxides. The interfacial reaction led to the depletion of Y, which was unfavorable for the deep desulfurization of Y during the refining process. In contrast, when Y-containing DD5 alloys were prepared by VIM using the Y_2O_3 crucible, only the Y-rich condensation shell was observed on the inner surface of the crucible.

References

1. Chen, Z.; Tan, Y.; Li, Y.; Zhao, J.; Song, S.; Li, P. Effect of oxygen on the wettability and interfacial reaction between the DD5 superalloy and ceramic shell. *Vacuum* **2023**, *215*, 112288. [CrossRef]
2. Chen, Z.; Wei, P.; Chen, H.; Chen, X.; Ruan, Y.; Zhou, W.; Lu, S. Laser Powder Bed Fusion of K418 Superalloy: Process, Microstructure, Texture Feature, and Mechanical Property. *Metals* **2022**, *12*, 611. [CrossRef]
3. Wei, D.; Liu, Y.; Wang, Y.; Wang, J.; Jiang, X. Normalized Parameter Creep Model of DD6 Nickel-Based Single Crystal Superalloy. *Metals* **2021**, *11*, 254. [CrossRef]
4. Xu, R.; Li, Y.; Yu, H. Creep Behavior and Deformation Mechanism of a Third-Generation Single Crystal Ni-Based Superalloy at 980 °C. *Metals* **2023**, *13*, 1541. [CrossRef]
5. Walston, S.; Cetel, A.; MacKay, R.; Ohara, K.; Duhl, D.; Dreshfield, R. Joint development of a fourth generation single crystal superalloy. In Proceedings of the 10th International Symposium on Superalloys, Champion, PA, USA, 19–23 September 2004.
6. Palleda, T.N.; Banoth, S.; Tanaka, M.; Murakami, H.; Kakehi, K. The role of yttrium micro-alloying on microstructure evolution and high-temperature mechanical properties of additively manufactured Inconel 718. *Mater. Des.* **2023**, *225*, 111567. [CrossRef]
7. Smialek, J. Origins of a Low-Sulfur Superalloy Al$_2$O$_3$ Scale Adhesion Map. *Crystals* **2021**, *11*, 60. [CrossRef]
8. Zhenxue, S.; Shizhong, L.; Mei, H.; Jiarong, L. Influence of yttrium addition on high temperature oxidation resistance of single crystal superalloy. *J. Rare Earths* **2013**, *31*, 795–799.
9. Tabata, C.; Kawagishi, K.; Uzuhashi, J.; Ohkubo, T.; Hono, K.; Yokokawa, T.; Harada, H.; Suzuki, S. Quantitative analysis of sulfur segregation at the oxide/substrate interface in Ni-base single crystal superalloy. *Scr. Mater.* **2021**, *194*, 113616. [CrossRef]
10. Zi, Y.; Meng, J.; Zhang, C.; Zhou, Y.; Ding, Y. Mechanisms of Rhenium on Wettability and Interactions Between Nickel-Base Superalloy Melt and Al$_2$O$_3$-Based Ceramic Material. *Acta Metall. Sin. (Engl. Lett.)* **2020**, *33*, 1021–1030. [CrossRef]
11. Gao, S.; Wang, M.; Xie, X.; Liu, M.; Bao, Y. Behavior of Nitrogen in GH4169 Superalloy Melt during Vacuum Induction Melting Using Returned Materials. *Metals* **2021**, *11*, 1119. [CrossRef]
12. Shmotin, Y.N.; Logunov, A.; Leshchenko, I.; Danilov, D. Development and research of a rhenium-free high-temperature nickel superalloy for the turbine rotor blades in aviation GTE. *Russ. Metall. (Met.)* **2016**, *2016*, 1214–1220. [CrossRef]
13. Jianxin, D.; Xingbo, L.; Bin, T.; Yaohe, H.U.; Zhichao, X.U.; Xishan, X. Effects of S on mechanical properties and microstructure of inconel 718 alloy. *Acta Met. Sin.* **1996**, *32*, 241–244.
14. Sun, C.; Huang, R.; Guo, J.; Hu, Z. Sulphur distribution in K24 cast nickel-base superalloy and its influence on mechanical properties. *High Temp. Technol.* **1988**, *6*, 145–148. [CrossRef]
15. Sidorov, V.; Rigin, V.; Min, P.; Folomeikin, Y.I. Removal of a sulfur impurity from complex nickel melts in vacuum. *Russ. Metall. (Met.)* **2015**, *2015*, 910–915. [CrossRef]
16. Lin, C.; Sheng, N.; Fan, S.; Sun, S.; Hou, G.; Yu, J.; Li, J.; Zhou, Y.; Sun, X. Effect of rare earth oxides on desulfurization reaction at CaO ceramic surface during smelting of Ni-based superalloy. *Appl. Surf. Sci.* **2023**, *620*, 156831. [CrossRef]
17. Zhan, X.; Wang, D.; Zhang, Z.; Zhang, J. Effect of trace sulfur on the hot corrosion resistance of Ni-base single crystal superalloy. *Corros. Sci.* **2023**, *224*, 111528. [CrossRef]
18. Sidorov, V.; Min, P. Refining a complex nickel alloy to remove a sulfur impurity during vacuum induction melting: Part II. *Russ. Metall. (Met.)* **2014**, *2014*, 987–991. [CrossRef]
19. Duan, S.-C.; Shi, X.; Wang, F.; Zhang, M.-C.; Li, B.; Yang, W.-S.; Guo, H.-J.; Guo, J. Investigation of desulfurization of Inconel 718 superalloys by ESR type slags with different TiO$_2$ content. *J. Mater. Res. Technol.* **2019**, *8*, 2508–2516. [CrossRef]
20. Xuan, W.; Du, L.; Song, G.; Zhang, X.; Zhang, H.; Ren, Z. Some new observations on interface reaction between nickel-based single crystal superalloy CMSX-4 and silicon oxide ceramic core. *Corros. Sci.* **2020**, *177*, 108969. [CrossRef]
21. Cui, J.; Li, B.; Liu, Z.; Qi, F.; Zhang, B.; Zhang, J. Numerical investigation of segregation evolution during the vacuum arc remelting process of Ni-based superalloy ingots. *Metals* **2021**, *11*, 2046. [CrossRef]
22. Wang, H.; Lei, Z.; Leng, X.; Xie, Y.; Zhu, H.; Huang, J. Temperature effect on the role of yttrium in oxidation behaviour of NiCrAl alloys. *Mater. High Temp.* **2018**, *35*, 371–377. [CrossRef]

23. Li, D.; Cosandey, F.; Maurer, G.; Foote, R.; Tien, J. Understanding the role of cerium during VIM refining of nickel-chromium and nickel-iron alloys. *Metall. Trans. B* **1982**, *13*, 603–611. [CrossRef]

24. Manman, W.; Yanhong, Y.; Daohong, W.; Zhihai, L.; Hongbin, Y.; Chuanyong, C. Deep deoxidation and desulfurization of cast superalloy K417G. *Rare Met. Mater. Eng.* **2018**, *47*, 3730–3734.

25. Bian, W.; Zhang, H.; Zhang, X.; Gao, M.; Li, J.; Li, Q.; Cui, Y.; Zhang, H. Comprehensive influence of Y on K417 superalloy: Purification, interactions among the alloy elements and high temperature properties. *Mater. Sci. Eng. A* **2019**, *755*, 190–200. [CrossRef]

26. Johnson, D.; Chihara, K.; Inui, H.; Yamaguchi, M. Microstructural control of TiAl–Mo–B alloys by directional solidification. *Acta Mater.* **1998**, *46*, 6529–6540. [CrossRef]

27. Liu, L.; Meng, J.; Liu, J.; Zou, M.; Zhang, H.; Sun, X.; Zhou, Y. Influences of Re on low-cycle fatigue behaviors of single crystal superalloys at intermediate temperature. *J. Mater. Sci. Technol.* **2019**, *35*, 1917–1924. [CrossRef]

28. Ford, D.; Ayan, B.; Catherine, M.F.R.; Ian, M.E.; Jones, C.N.; Leyland, S.P.; Irwin, S. *The Distribution and Retention of Yttrium and Lanthanum in Cast Single Crystal Superalloys*; The Minerals, Metals & Materials Society: Pittsburgh, PA, USA, 2020.

29. Zhang, H.; Tang, X.; Zhou, L.; Gao, M.; Zhou, C.; Zhang, H. Interactions between Ni-44Ti-5Al-2Nb-Mo alloy and oxide ceramics during directional solidification process. *J. Mater. Sci.* **2012**, *47*, 6451–6458. [CrossRef]

30. Li, J.-P.; Zhang, H.-R.; Gao, M.; Li, Q.-L.; Zhang, J.; Yang, B.; Zhang, H. Mechanism of yttrium in deep desulfurization of NiCoCrAlY alloy during vacuum induction melting process. *Rare Met.* **2022**, *41*, 218–225. [CrossRef]

31. Cao, S.; Yang, Y.; Chen, B.; Liu, K.; Ma, Y.; Ding, L.; Shi, J. Influence of yttrium on purification and carbide precipitation of superalloy K4169. *J. Mater. Sci. Technol.* **2021**, *86*, 260–270. [CrossRef]

32. Peng, Y.; Li, J.; Li, S.; Chen, Y.; Li, Z.; Guo, W.; Xiong, J. Microstructure evaluation and fracture mechanism of dissimilar diffusion bonded joint of single crystal superalloy DD5 and polycrystalline superalloy GH4169. *Mater. Charact.* **2022**, *189*, 111999. [CrossRef]

33. *GB/T 20123-2006*; Steel and Iron-Determination of Total Carbon and Sulfur Content, Infrared Absorption Method after Combustion in an Induction Furnace. Standardization Administration of China: Beijing, China, 2006.

34. Matysiak, H.; Zagorska, M.; Andersson, J.; Balkowiec, A.; Cygan, R.; Rasinski, M.; Pisarek, M.; Andrzejczuk, M.; Kubiak, K.; Kurzydlowski, K.J. Microstructure of Haynes® 282® superalloy after vacuum induction melting and investment casting of thin-walled components. *Materials* **2013**, *6*, 5016–5037. [CrossRef]

35. Fortuna, S.; Gurianov, D.; Nikonov, S.; Osipovich, K.; Kolubaev, E. On the Control of Elemental Composition, Macro-, and Microstructure of Directionally Solidified Additive Products from Nickel-Based Alloy. *Metals* **2023**, *13*, 1457. [CrossRef]

36. Du, T.; Wang, L.; Liu, A.; Wu, Y.; Zhang, Y. Thermodynamics and phase equilibria for cerium and yttrium in the presence of oxygen and sulphur in nickel-base solutions. *J. Alloys Compd.* **1993**, *193*, 38–40. [CrossRef]

37. Schumann, E.; Yang, J.; Graham, M. Direct observation of the interaction of yttrium and sulfur in oxidized NiAl. *Scr. Mater.* **1996**, *34*, 1365–1370. [CrossRef]

38. Wang, H.; Shang, G.; Liao, J.; Yang, B.; Yuan, C. Experimental investigations and thermodynamic calculations of the interface reactions between ceramic moulds and Ni-based single-crystal superalloys: Role of solubility of Y in the LaAlO$_3$ phase. *Ceram. Int.* **2018**, *44*, 7667–7673. [CrossRef]

39. Li, X.; Zhao, Y.; Wang, L.; Long, X.; Chen, C.; Qin, Z. Study on the stability of different refractories during the melting process of a K4169 Ni-based superalloy. *Ceram. Int.* **2023**, *49*, 29573–29583. [CrossRef]